Journal of Harbin Engineering University
ISSN: 1006-7043

Vol 47 No. 04
Oct 2026

Size-dependent Hygrothermal Buckling of Porous Functionally Graded Nanoplates on Kerr Foundations via OVFSDT and NSGT

Nawal A. Alshehri[1]

[1] Department of Mathematics, College of Science, Taif University, P.O. Box 11099, Taif 21944, Saudi Arabia.
Email ID: nalshehri@tu.edu.sa

Abstract

Porous functionally graded (FG) nanoplates are candidate elements of thermal-protection, sensing and actuation systems in aerospace vehicles, where temperature and moisture act together. The hygrothermal and mechanical buckling of such nanoplates resting on a three-parameter Kerr elastic foundation is studied with a one-variable first-order shear deformation theory (OVFSDT) combined with the nonlocal strain gradient theory (NSGT). The kinematics are written about the physical neutral surface, which removes the stretching–bending coupling of the FG section and allows the problem to be reduced exactly to a single unknown, the bending deflection. It is shown that the relation between the shear and bending deflections survives the nonlocal strain gradient operators unchanged, so the size-dependent stability problem is governed by one fourth-order equation. Closed-form critical loads are obtained by the Navier procedure for simply-supported plates under uniaxial and biaxial compression, and critical temperature rises are obtained for uniform, linear and nonlinear (steady heat-conduction) hygrothermal distributions through the thickness. Even and uneven porosity distributions are considered. In the classical limit the present solution reproduces the published thermal-buckling results of Yaghoobi and Torabi to all reported digits, and is practically identical to the mechanical results of Thai and Kim for homogeneous plates. New benchmark tables and parametric figures show the competing softening (nonlocal) and hardening (strain-gradient) effects, the role of the upper-spring layer of the Kerr model, the influence of porosity, and the reduction of the critical temperature with moisture concentration.

Keywords: Hygrothermal buckling, Porous functionally graded nanoplates, One-variable first-order shear deformation theory, Nonlocal strain gradient theory, Kerr foundation, Physical neutral surface.

1. Introduction

Aerospace vehicles operate in some of the most severe thermal environments in engineering. The skins of re-entry and hypersonic vehicles, the combustion chambers and nozzles of rocket engines, and the hot sections of gas-turbine engines all carry large temperature differences across thin walls. Functionally graded materials (FGMs) were conceived for exactly this situation. The concept was proposed in Japan in the mid-1980s as a thermal-barrier material for the airframe of a space plane, whose outer face had to withstand a very high surface temperature while the inner face remained far cooler [1]. In an FGM the composition varies continuously from a heat-resistant ceramic on the hot face to a tough, conductive metal on the cold face. This smooth gradation removes the sharp interfaces of conventional layered coatings, and with them the stress concentrations and delamination that repeated thermal cycling produces at such interfaces.

Thin FGM panels in aerospace structures are loaded mainly in their own plane, by aerodynamic and inertial forces and by restrained thermal expansion. Buckling is therefore a primary design limit, and its prediction must account for the graded properties. Reddy [2] established the basic analysis of FG plates with higher-order shear deformation theory. Thermal buckling of FG plates has since been studied with classical, first-order and higher-order theories [3–6], and closed-form mechanical buckling solutions for thick FG plates on elastic foundations were given by Thai and Kim [7].

Temperature is rarely the only environmental load in flight. A typical mission takes an aircraft structure from humid ground conditions to cold, dry cruise altitude and back, and high-speed flight adds aerodynamic heating. Absorbed moisture swells the material and, like temperature, produces compressive in-plane forces in a restrained panel. The combined hygrothermal environment therefore erodes the buckling margin, and both effects must be designed for

together. Hygrothermal effects on the buckling of laminated plates were examined early by Sai Ram and Sinha [17], and on laminated and FG plates resting on elastic foundations in [18, 19]. The present authors recently treated the hygrothermo-mechanical buckling of FG plates on Winkler–Pasternak foundations with a quasi-3D model including thickness stretching [20].

Aerospace systems also rely increasingly on components at the micro- and nanoscale: sensors and actuators for structural health monitoring, micro- and nano-electromechanical devices in guidance and avionics, and thin protective and thermal-barrier films. Graded nanoplates are natural building blocks for such devices, and they experience the same thermal and moisture environment as the host structure. At these scales the classical continuum does not predict stiffness correctly. Eringen's nonlocal theory [25] captures stiffness softening and has been applied to the bending, buckling and vibration of beams and plates [26–28]. The nonlocal strain gradient theory (NSGT) of Lim et al. [29] adds a material length scale and can predict both softening and hardening; it has been used for the buckling of nanobeams [30] and for hygrothermal problems of FG nanostructures [31].

Design studies for aerospace components require many evaluations of the critical load, for example in parametric sizing and optimization. Plate theories with few unknowns and closed-form solutions are valuable in this setting. First-order shear deformation theory, introduced by Reissner [8] and Mindlin [9], is the simplest theory that accounts for transverse shear. Shimpi [10] proposed a refined plate theory in which the transverse deflection is split into bending and shear components, and Shimpi et al. [11] later reformulated first-order theory in the same way. For isotropic plates the equilibrium equations then relate the two components, and the theory collapses to a single unknown.

In aerospace applications the elastic medium beneath a plate may represent a substrate, an adhesive bond layer, the soft core of a sandwich panel, or the interface between a coating and the structure it protects. Such media are commonly modelled by the two-parameter Pasternak foundation [12], or by the three-parameter Kerr foundation [13], which adds an upper spring layer above the shear layer and so can represent a compliant bond between the plate and the shear-carrying medium. Exact solutions for Mindlin plates on Pasternak foundations were obtained by Akhavan et al. [14], and simple and mixed first-order theories for homogeneous and FG plates on elastic foundations were developed by Zenkour and co-workers [15, 16].

Two further issues are important for FG plates under thermal load. First, the material gradation shifts the neutral surface away from the mid-plane and couples stretching and bending. Under in-plane loads this coupling can bend a simply-supported plate before any bifurcation occurs [22]. Writing the kinematics about the physical neutral surface removes the coupling for constant Poisson's ratio [21] and makes the bifurcation analysis consistent. Second, powder-based and spray-based fabrication routes for FGMs leave porosity, whose amount and distribution reduce stiffness [23, 24] and must be accounted for in a realistic design.

Porous FG nanoplates in hygrothermal environments on Kerr foundations have been studied for free vibration with NSGT and a second-order theory [32], for shear buckling with a quasi-3D theory and Eringen's model [33], and for buckling with a five-variable quasi-3D theory [34]. Free vibration of porous FG nanoplates on Pasternak foundations with NSGT and classical, first- and third-order theories was reported in [35]. All of these works use displacement fields with three to six unknowns. The one-variable first-order theory has been combined with NSGT for piezo-magnetoelectric nanoplates [36]. It has not, to the authors' knowledge, been applied to FG plates, because the stretching–bending coupling of an FG section prevents the reduction to one variable.

This paper bridges the existing gap by providing a compact design tool for porous functionally graded nanoplates in aerospace hygrothermal environments. By formulating a neutral-surface-based one-variable first-order shear deformation theory (**OVFSDT**), the problem is successfully reduced to a single bending deflection equation, as the bending-shear relation remains unaffected by the nonlocal strain gradient theory (**NSGT**) operators. Closed-form critical loads and temperature rises—incorporating mechanical, uniform, linear, and steady-state nonlinear thermal distributions on a **Kerr foundation**—are derived and validated against published benchmarks, offering new comprehensive benchmark tables and parametric figures.

2. Mathematical Formulation

Consider a rectangular porous FG nanoplate of length a, width b and thickness h, resting on a Kerr foundation

and exposed to a temperature rise $T(z)$ and a moisture-concentration rise $C(z)$ (Fig. 1). The top surface ($z = h/2$) is ceramic and the bottom surface ($z = -h/2$) is metal.

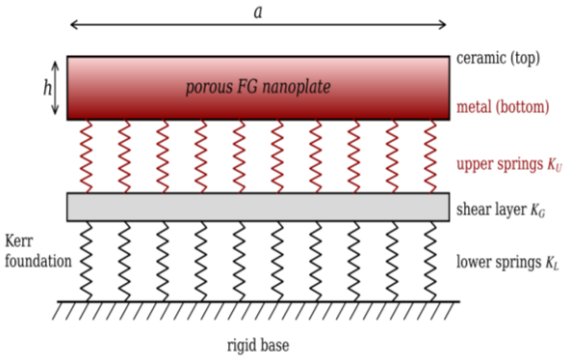


Fig. 1. Geometry of a porous FG nanoplate resting on a three-parameter Kerr foundation.

2.1 Porous FG Material and the Physical Neutral Surface

Young's modulus follows a modified power law with even or uneven porosity of volume fraction e [23]:

$$E(z) = E_m + (E_c - E_m)\left(\frac{z}{h} + \frac{1}{2}\right)^k - \frac{e}{2}(E_c + E_m)\,\Phi(z), \qquad \Phi(z) = \begin{cases} 1, & \text{even} \\ 1 - \frac{2|z|}{h}, & \text{uneven} \end{cases} \tag{1}$$

The thermal expansion $\alpha(z)$, moisture expansion $\beta(z)$ and thermal conductivity $K(z)$ follow the same power law without the porosity term, and Poisson's ratio ν is constant. Because $E(z)$ is not symmetric, the stretching–bending coupling vanishes only about the physical neutral surface [21]:

$$z_0 = \frac{\int_{-h/2}^{h/2} E(z)\, z\, dz}{\int_{-h/2}^{h/2} E(z)\, dz}, \qquad \bar{z} = z - z_0 \tag{2}$$

2.2 Kerr Foundation

The Kerr model consists of a lower spring layer of stiffness K_L, a shear layer of stiffness K_G and an upper spring layer of stiffness K_U [13]. The foundation reaction R_f satisfies

$$\left(1 + \frac{K_L}{K_U}\right) R_f - \frac{K_G}{K_U}\nabla^2 R_f = K_L\, w - K_G \nabla^2 w \tag{3}$$

The Pasternak model [12] is recovered as $K_U \to \infty$, and the Winkler model when, in addition, $K_G = 0$.

2.3 One-variable First-Order Kinematics

Following Shimpi et al. [11], the transverse deflection is split into a bending part w_b and a shear part w_s, and the in-plane displacements are measured from the neutral surface:

$$u = u_0 - \bar{z}\,\frac{\partial w_b}{\partial x}, \qquad v = v_0 - \bar{z}\,\frac{\partial w_b}{\partial y}, \qquad w = w_b(x,y) + w_s(x,y) \tag{4}$$

The non-zero strains are

$$\begin{Bmatrix} \varepsilon_x \\ \varepsilon_y \\ \gamma_{xy} \end{Bmatrix} = \begin{Bmatrix} \partial u_0/\partial x \\ \partial v_0/\partial y \\ \partial u_0/\partial y + \partial v_0/\partial x \end{Bmatrix} - \bar{z} \begin{Bmatrix} \partial^2 w_b/\partial x^2 \\ \partial^2 w_b/\partial y^2 \\ 2\,\partial^2 w_b/\partial x\,\partial y \end{Bmatrix}, \qquad \gamma_{xz} = \frac{\partial w_s}{\partial x}, \qquad \gamma_{yz} = \frac{\partial w_s}{\partial y} \tag{5}$$

Bending curvatures depend only on w_b and transverse shear strains only on w_s. A shear correction factor $\kappa_s = 5/6$ is used for the shear stiffness, as in any first-order theory.

2.4 Nonlocal Strain Gradient Constitutive Relations

The local stresses are

$$\sigma_{ij}^L = C_{ijkl}(z)[\varepsilon_{kl} - (\alpha(z)\,T(z) + \beta(z)\,C(z))\,\delta_{kl}] \tag{6}$$

In the NSGT [29], with nonlocal parameter $\mu = (e_0 a)^2$ and strain-gradient length scale ℓ, the stress resultants satisfy

$$(1 - \mu\nabla^2)\{M_x, M_y, M_{xy}\} = (1 - \ell^2\nabla^2)\{M_x^L, M_y^L, M_{xy}^L\}, \qquad (1 - \mu\nabla^2)\{Q_x, Q_y\} = (1 - \ell^2\nabla^2)\,\kappa_s A_{55}\left\{\frac{\partial w_s}{\partial x}, \frac{\partial w_s}{\partial y}\right\} \tag{7}$$

with the local moments

$$M_x^L = -D\left(\frac{\partial^2 w_b}{\partial x^2} + \nu\frac{\partial^2 w_b}{\partial y^2}\right), \quad M_y^L = -D\left(\frac{\partial^2 w_b}{\partial y^2} + \nu\frac{\partial^2 w_b}{\partial x^2}\right), \quad M_{xy}^L = -D(1-\nu)\frac{\partial^2 w_b}{\partial x\,\partial y} \tag{8}$$

The rigidities, computed about the neutral surface, are

$$D = \int_{-h/2}^{h/2} \frac{E(z)}{1-\nu^2}(z - z_0)^2\, dz, \qquad A_{55} = \int_{-h/2}^{h/2} \frac{E(z)}{2(1+\nu)}\, dz \tag{9}$$

By the definition of z_0 the coupling rigidity vanishes, so the in-plane displacements u_0 and v_0 decouple from the bending problem.

2.5 Pre-buckling state

Before buckling the plate is in a uniform membrane state. The in-plane forces are $N_x^0 = -N_1$ and $N_y^0 = -N_2$ (compression positive). For hygrothermal loading $N_1 = N_2 = N^{HT}$, with

$$N^{HT} = \int_{-h/2}^{h/2} \frac{E(z)}{1-\nu}[\alpha(z)\,T(z) + \beta(z)\,C(z)]dz \tag{10}$$

For non-uniform distributions a hygrothermal moment also exists about the neutral surface. As is customary in bifurcation analyses of FG plates [3, 6], its pre-buckling bending effect is neglected; the results for linear and nonlinear loading should be read with this assumption [22].

2.6 Stability Equations

The principle of virtual work (adjacent-equilibrium criterion), with the virtual variations of w_b and w_s taken independently, gives

$$\delta w_b: \quad \frac{\partial^2 M_x}{\partial x^2} + 2\frac{\partial^2 M_{xy}}{\partial x\,\partial y} + \frac{\partial^2 M_y}{\partial y^2} + \bar{N}(w) - R_f = 0 \quad (11)$$

$$\delta w_s: \quad \frac{\partial Q_x}{\partial x} + \frac{\partial Q_y}{\partial y} + \bar{N}(w) - R_f = 0, \qquad \bar{N}(w) = N_x^0\frac{\partial^2 w}{\partial x^2} + N_y^0\frac{\partial^2 w}{\partial y^2} \quad (12)$$

2.7 Reduction to One Variable

Applying the operator $(1-\mu\nabla^2)$ to both equations and substituting Eqs. (7) and (8) gives

$$-(1-\ell^2\nabla^2)\,D\nabla^4 w_b + (1-\mu\nabla^2)\left[\bar{N}(w) - R_f\right] = 0 \quad (13)$$

$$(1-\ell^2\nabla^2)\,\kappa_s A_{55}\nabla^2 w_s + (1-\mu\nabla^2)\left[\bar{N}(w) - R_f\right] = 0 \quad (14)$$

Subtracting the two equations removes the loads and the foundation entirely:

$$(1-\ell^2\nabla^2)[D\nabla^4 w_b + \kappa_s A_{55}\nabla^2 w_s] = 0 \quad \Rightarrow \quad w_s = -\frac{D}{\kappa_s A_{55}}\nabla^2 w_b \quad (15)$$

The bending–shear relation is therefore identical to the local one [11]: the nonlocal and strain-gradient operators do not alter it. Substituting it back gives the single governing equation of the size-dependent stability problem:

$$(1-\ell^2\nabla^2)\,D\nabla^4 w_b = (1-\mu\nabla^2)\left(1 - \frac{D}{\kappa_s A_{55}}\nabla^2\right)\left[\bar{N}(w_b) - \hat{R}_f(w_b)\right] \quad (16)$$

Here $\hat{R}_f$ is the Kerr reaction expressed through w_b. Only one unknown remains, compared with six in the quasi-3D model of [20] and five in conventional first-order theory.

3. Closed-form Solution

For a plate simply supported on all edges, the Navier form

$$w_b = W_{mn}\sin(\lambda_m x)\sin(\eta_n y), \qquad \lambda_m = \frac{m\pi}{a}, \quad \eta_n = \frac{n\pi}{b}, \quad \alpha_{mn}^2 = \lambda_m^2 + \eta_n^2 \quad (17)$$

satisfies the boundary conditions exactly; w_s and w share the same shape, with $w = (1+S)\,w_b$. The shear parameter S and the Kerr stiffness $\widehat{K}$ of mode (m,n) are

$$S = \frac{D\,\alpha_{mn}^2}{\kappa_s A_{55}}, \qquad \widehat{K} = \frac{K_L + K_G\,\alpha_{mn}^2}{1 + K_L/K_U + K_G\,\alpha_{mn}^2/K_U} \quad (18)$$

3.1 Mechanical Buckling

With $N_1 = N$ and $N_2 = RN$, where R is the load ratio ($R = 0$ uniaxial, $R = 1$ biaxial), Eq. (16) gives

$$N_{cr} = \min_{m,n}\ \frac{1}{\lambda_m^2 + R\,\eta_n^2}\left[\frac{(1+\ell^2\alpha_{mn}^2)\,D\,\alpha_{mn}^4}{(1+\mu\,\alpha_{mn}^2)(1+S)} + \widehat{K}\right] \quad (19)$$

This expression contains several limits as special cases. With $\mu = \ell = 0$ it is the local first-order solution. With $S \to 0$ it reduces to the classical plate result, and with $\ell = 0$ to Eringen's nonlocal result, in which the stiffness is divided by $(1+\mu\alpha^2)$. The factor $(1+\ell^2\alpha^2)/(1+\mu\alpha^2)$ shows directly that the plate softens when $\mu > \ell^2$ and hardens when $\ell^2 > \mu$.

With $\mu > 0$, the product $(1+\mu\alpha^2)(1+S)$ grows like α^4 for short wavelengths, so very high modes would give a vanishing load. Such modes have half-wavelengths shorter than the nonlocal length $\sqrt{\mu}$ and lie outside the validity of the continuum model. The search is therefore limited to $m, n \le 3$, which keeps every half-wavelength above twice $\sqrt{\mu}$ for the parameter ranges used.

3.2 Hygrothermal Buckling

The plate buckles when N^{HT} reaches N_{cr} with $R = 1$. Three distributions through the thickness are considered.

Uniform hygrothermal rise (UHTR):

$$T(z) = \Delta T, \qquad C(z) = \Delta C \quad (20)$$

Linear hygrothermal distribution (LHTD), where T_m is the metal-surface temperature rise and $C_m = 0$:

$$T(z) = \Delta T\left(\frac{z}{h} + \frac{1}{2}\right) + T_m, \qquad C(z) = \Delta C\left(\frac{z}{h} + \frac{1}{2}\right) + C_m \quad (21)$$

Nonlinear hygrothermal distribution (NHTD). The temperature follows the steady one-dimensional heat-conduction equation $d/dz\,[K(z)\,dT/dz] = 0$ with $T(-h/2) = T_m$ and $T(h/2) = T_m + \Delta T$:

$$T(z) = T_m + \Delta T\,g(z), \qquad g(z) = \frac{\int_{-h/2}^{z} d\zeta/K(\zeta)}{\int_{-h/2}^{h/2} d\zeta/K(\zeta)}, \qquad C(z) = \Delta C\,g(z) \quad (22)$$

The moisture is assumed to follow the same normalized profile $g(z)$, since graded diffusivity data for the constituents are not available. For a homogeneous plate $g(z)$ is linear, so NHTD and LHTD coincide, which serves as a check. This replaces the assumed hyperbolic profile used in [20] with one derived from the conduction equation.

In every case N^{HT} is linear in ΔT and ΔC, so the critical temperature rise is explicit:

$$\Delta T_{cr} = \frac{N_{cr}(R=1) - P_C\,\Delta C - P_T\,T_m}{P_T^g} \tag{23}$$

with the hygrothermal stiffnesses

$$P_T^g = \int_{-h/2}^{h/2} \frac{E\,\alpha\,g}{1-\nu}\,dz, \qquad P_T = \int_{-h/2}^{h/2} \frac{E\,\alpha}{1-\nu}\,dz, \qquad P_C = \int_{-h/2}^{h/2} \frac{E\,\beta\,g}{1-\nu}\,dz \tag{24}$$

where $g = 1$ for UHTR, $g = z/h + 1/2$ for LHTD and g from Eq. (22) for NHTD ($T_m = 0$ for UHTR). A negative ΔT_{cr} means that the moisture alone is enough to buckle the plate.

4. Numerical Results

The plates are made of alumina (ceramic, top) and aluminium (metal, bottom), with the properties listed in Table 1; $\nu = 0.3$ and $\kappa_s = 5/6$ throughout. The moisture coefficients follow [18, 20], with $\beta = 0$ for alumina. ΔC is reported in wt.% and converted to a mass fraction in the calculation.

Table 1: Material properties of the constituents.

Constituent	E **(GPa)**	α **(1/K)**	β **(per unit mass fraction)**	K **(W/m·K)**
Alumina, Al_2O_3 (ceramic)	380	7.4×10^{-6}	0	10.4
Aluminium, Al (metal)	70	23×10^{-6}	0.33	204

The following dimensionless quantities are used:

$$\bar{N}_{cr} = \frac{N_{cr}\,a^2}{E_m h^3}, \quad \bar{\mu} = \frac{\mu}{a^2}, \quad \bar{\ell} = \frac{\ell}{a}, \quad \kappa_L = \frac{K_L a^4}{D_c}, \quad \kappa_G = \frac{K_G a^2}{D_c}, \quad \kappa_U = \frac{K_U a^4}{D_c}, \quad D_c = \frac{E_c h^3}{12(1-\nu^2)} \tag{25}$$

In the validation tables the foundation parameters follow the normalization of each reference: κ_W and κ_P are normalized by $D_m = E_m h^3/12(1-\nu^2)$ in Table 2, as in [7], and by D_c in Tables 3 and 4, as in [6]. For a nanoplate of side $a = 10$ nm, $\bar{\mu} = 0.02$ corresponds to $e_0 a \approx 1.4$ nm and $\bar{\ell} = 0.1$ to $\ell = 1$ nm. $T_m = 5$ K is used for linear and nonlinear loading.

4.1 Validation

Mechanical buckling. Table 2 compares $\bar{N}_{cr}$ of perfect FG square plates ($a/h = 10$, $\bar{\mu} = \bar{\ell} = 0$) with the closed-form results of Thai and Kim [7]. For $k = 0$ and $k = 1$ the two are practically identical, agreeing to four significant figures. At $k = 5$ and $k = 10$ the present values are slightly higher, which reflects the different shear-strain distribution of the refined theory in [7]. Mode switching to $(m, n) = (2,1)$ for $\kappa_W = 1000$, $\kappa_P = 100$ under uniaxial load is captured as in [7].

Table 2: Critical buckling load $\bar{N}_{cr}$ of perfect FG square plates on a Winkler–Pasternak foundation ($a/h = 10$, $\bar{\mu} = \bar{\ell} = 0$).

κ_W	κ_P	R	Source	$k = 0$	$k = 0.5$	$k = 1$	$k = 2$	$k = 5$	$k = 10$
0	0	0	Ref. [7]	18.5785	12.1229	9.3391	7.2631	6.0353	5.4528
			Present	18.5778	12.1138	9.3388	7.2830	6.1017	5.5189
0	0	1	Ref. [7]	9.2893	6.0615	4.6695	3.6315	3.0177	2.7264
			Present	9.2889	6.0569	4.6694	3.6415	3.0508	2.7594
100	10	0	Ref. [7]	21.3379	14.8823	12.0985	10.0224	8.7947	8.2122
			Present	21.3372	14.8732	12.0982	10.0423	8.8610	8.2782
100	10	1	Ref. [7]	10.6689	7.4411	6.0492	5.0112	4.3973	4.1061
			Present	10.6686	7.4366	6.0491	5.0212	4.4305	4.1391
1000	100	0	Ref. [7]	40.6477	31.4605	27.4319	24.3470	22.3602	21.4516

κ_W	κ_P	R	Source	$k=0$	$k=0.5$	$k=1$	$k=2$	$k=5$	$k=10$
			Present	40.6422	31.4277	27.4295	24.4134	22.5767	21.6627
1000	100	1	Ref. [7]	23.0860	19.8582	18.4663	17.4283	16.8144	16.5232
			Present	23.0857	19.8537	18.4662	17.4383	16.8476	16.5562

Thermal buckling. Tables 3 and 4 compare the critical temperature difference, expressed as $\Delta T_{cr} \times 10^{-3}$, with Yaghoobi and Torabi [6] for uniform and linear temperature rise. The two agree to all five reported digits for every k, a/h and foundation. This exact agreement is expected: [6] uses first-order theory about the neutral surface, and for simply-supported plates the one-variable reduction is exact. The present formulation therefore reaches the same answer with one unknown instead of three.

Table 3: Critical temperature difference $\Delta T_{cr} \times 10^{-3}$ of perfect FG square plates under uniform temperature rise.

κ_W	κ_P	a/h	Source	$k=0$	$k=1$	$k=5$	$k=10$
0	0	5	Ref. [6]	5.58069	2.67039	2.35948	2.36822
			Present	5.58069	2.67039	2.35948	2.36822
0	0	10	Ref. [6]	1.61862	0.75837	0.68678	0.70108
			Present	1.61862	0.75837	0.68678	0.70108
0	0	20	Ref. [6]	0.42153	0.19626	0.17905	0.18373
			Present	0.42153	0.19626	0.17905	0.18373
10	0	10	Ref. [6]	1.66251	0.79928	0.74347	0.76507
			Present	1.66251	0.79928	0.74347	0.76507
10	10	5	Ref. [6]	9.22123	6.06356	7.06257	7.67626
			Present	9.22123	6.06356	7.06257	7.67626
10	10	10	Ref. [6]	2.52876	1.60667	1.86255	2.02809
			Present	2.52876	1.60667	1.86255	2.02809
10	10	20	Ref. [6]	0.64907	0.40834	0.47299	0.51548
			Present	0.64907	0.40834	0.47299	0.51548

Table 4: Critical temperature difference $\Delta T_{cr} \times 10^{-3}$ of perfect FG square plates under linear temperature distribution ($T_m = 5$ K).

κ_W	κ_P	a/h	Source	$k=0$	$k=1$	$k=5$	$k=10$
0	0	5	Ref. [6]	11.15138	4.99885	4.05274	4.18778
			Present	11.15138	4.99885	4.05274	4.18778
0	0	10	Ref. [6]	3.22725	1.41292	1.17354	1.23350
			Present	3.22725	1.41292	1.17354	1.23350
0	0	20	Ref. [6]	0.83307	0.35871	0.29959	0.31672
			Present	0.83307	0.35871	0.29959	0.31672
10	0	10	Ref. [6]	3.31502	1.48964	1.27113	1.34688
			Present	3.31502	1.48964	1.27113	1.34688
10	10	5	Ref. [6]	18.43246	11.36263	12.14814	13.59396
			Present	18.43246	11.36263	12.14814	13.59396
10	10	10	Ref. [6]	5.04752	3.00387	3.19739	3.58504
			Present	5.04752	3.00387	3.19739	3.58504

κ_W	κ_P	a/h	Source	$k=0$	$k=1$	$k=5$	$k=10$
10	10	20	Ref. [6]	1.28814	0.75645	0.80555	0.90460
			Present	1.28814	0.75645	0.80555	0.90460

The nonlocal and Kerr parts are checked by limits. Setting $K_U \to \infty$ recovers the Pasternak values (Fig. 5), and $K_U \to 0$ removes the foundation. Setting $\ell = 0$ and $S \to 0$ recovers Eringen's classical nonlocal plate result. With homogeneous material the nonlinear temperature profile reduces to the linear one, and Table 8 shows identical LHTD and NHTD values for $k = 0$.

4.2 Benchmark Results for Porous FG Nanoplates

Tables 5–8 give new results for future comparison. Unless stated otherwise the plate is square, the porosity is even with $e = 0.1$, and the Kerr foundation is $(\kappa_L, \kappa_G, \kappa_U) = (100,10,100)$.

Size effects. Table 5 lists $\bar{N}_{cr}$ for $a/h = 10$. Without a foundation, $\bar{\mu} = 0.02$ lowers the uniaxial load of the ceramic plate from 17.4778 to 12.5309, while $\bar{\ell} = 0.1$ raises it to 20.9278. With both, the load falls to 15.0043, which is the local value multiplied by the factor $(1 + \ell^2\alpha^2)/(1 + \mu\alpha^2) = 0.858$ for the (1, 1) mode. The nonlocal and strain-gradient parameters therefore act as independent softening and hardening multipliers on the plate stiffness, while the foundation term is unaffected by them. This is why the foundation becomes relatively more important when $\bar{\mu} > 0$, and why the governing mode can switch to (2, 1) or (3, 1) on a stiff Pasternak foundation.

Table 5: Critical buckling load $\bar{N}_{cr}$ of even-porous FG square nanoplates ($e = 0.1$, $a/h = 10$); $R = 0$ uniaxial, $R = 1$ biaxial.

Foundation	$\bar{\mu}$	$\bar{\ell}$	R	$k=0$	$k=1$	$k=5$	$k=10$
None	0	0	0	17.4778	8.0505	4.6488	4.1894
	0	0	1	8.7389	4.0253	2.3244	2.0947
	0.02	0	0	12.5309	5.7719	3.3330	3.0036
	0.02	0	1	6.2654	2.8859	1.6665	1.5018
	0	0.1	0	20.9278	9.6397	5.5665	5.0164
	0	0.1	1	10.4639	4.8198	2.7832	2.5082
	0.02	0.1	0	15.0043	6.9112	3.9909	3.5965
	0.02	0.1	1	7.5022	3.4556	1.9955	1.7983
Pasternak (100, 10)	0	0	0	32.4572	19.2832	14.2190	13.4750
	0	0	1	16.2286	11.5149	9.8141	9.5844
	0.02	0	0	19.5356	12.4902	9.6874	9.2344
	0.02	0	1	13.7551	10.3756	8.5107	8.0420
	0	0.1	0	35.9072	24.6190	17.5480	16.4368
	0	0.1	1	17.9536	12.3095	10.2729	9.9979
	0.02	0.1	0	26.4780	16.3501	12.5437	11.9844
	0.02	0.1	1	14.9918	10.9453	9.4851	9.2879
Kerr (100, 10, 100)	0	0	0	21.2472	11.8199	7.8234	7.0794
	0	0	1	10.6236	5.9100	4.2091	3.9794
	0.02	0	0	13.8028	6.9195	4.1167	3.6637
	0.02	0	1	8.1501	4.7706	3.5254	3.0566
	0	0.1	0	24.6972	13.4091	9.3359	8.7858
	0	0.1	1	12.3486	6.7045	4.6679	4.3929

Foundation	$\bar{\mu}$	$\bar{\ell}$	R	$k=0$	$k=1$	$k=5$	$k=10$
	0.02	0.1	0	18.7738	9.9544	6.1481	5.5888
	0.02	0.1	1	9.3869	5.3403	3.8802	3.6830

Porosity and the upper Kerr layer. Table 6 isolates porosity and the foundation model for $k=2$. Even porosity with $e=0.2$ leaves the unsupported plate with only about three-fifths of the critical load of the perfect plate, whereas uneven porosity of the same amount retains nearly nine-tenths of it: uneven pores sit near the mid-surface, where they contribute little to bending stiffness. The upper spring layer of the Kerr model acts in series with the lower springs, so the Kerr foundation is always softer than the Pasternak foundation with the same κ_L and κ_G. At $\kappa_U=10$ it raises the load only marginally above the unsupported value, whereas the Pasternak limit raises it about two and a half times.

Table 6: Effect of porosity and foundation model on $\bar{N}_{cr}$ ($k=2$, $a/h=10$, $\bar{\mu}=0.02$, $\bar{\ell}=0.1$, uniaxial). All foundations use $\kappa_L=100$ and, where present, $\kappa_G=10$.

Porosity	e	None	Winkler	Pasternak	Kerr, $\kappa_U=1000$	Kerr, $\kappa_U=100$	Kerr, $\kappa_U=10$
Perfect	0	6.2523	9.2619	15.4759	12.6925	9.0803	6.7396
Even	0.1	5.0272	7.7255	13.9395	11.1562	7.5439	5.5145
Even	0.2	3.6987	6.0555	12.2695	9.4862	5.8739	4.1860
Uneven	0.1	5.8772	8.7792	14.9932	12.2099	8.5976	6.3645
Uneven	0.2	5.4828	8.2735	14.4875	11.7041	8.0919	5.9701

Moisture. Table 7 gives ΔT_{cr} under uniform hygrothermal rise for $a/h=20$. Because alumina absorbs no moisture ($\beta_c=0$), the ceramic plate ($k=0$) is insensitive to ΔC. For FG plates every 0.2 wt.% of moisture lowers ΔT_{cr} by about 18–26 K; for $k=1$ and local material, $\Delta C=0.4$ wt.% reduces ΔT_{cr} from 276.85 K to 239.63 K. The size effects scale the critical temperature by the same factors as the mechanical load, since N^{HT} does not depend on μ or ℓ.

Table 7: Critical temperature rise ΔT_{cr} (K) under uniform hygrothermal rise (even porosity $e=0.1$, $a/h=20$, Kerr (100, 10, 100)).

ΔC (wt.%)	$\bar{\mu}$	$\bar{\ell}$	$k=0$	$k=1$	$k=5$	$k=10$
0.0	0	0	508.81	276.85	306.80	346.26
	0.02	0	389.49	222.92	258.00	293.54
	0	0.1	592.01	314.46	340.83	383.03
	0.02	0.1	449.15	249.88	282.40	319.90
0.2	0	0	508.81	258.24	282.56	320.37
	0.02	0	389.49	204.31	233.77	267.65
	0	0.1	592.01	295.85	316.59	357.14
	0.02	0.1	449.15	231.27	258.17	294.01
0.4	0	0	508.81	239.63	258.33	294.48
	0.02	0	389.49	185.70	209.54	241.76
	0	0.1	592.01	277.24	292.36	331.25
	0.02	0.1	449.15	212.67	233.94	268.12

Loading type. Table 8 compares the three distributions at $\Delta C = 0.2$ wt.%. Linear loading roughly doubles ΔT_{cr} relative to uniform loading, because only half of the top-to-bottom difference acts on average. The conduction-based nonlinear profile raises it further, to between two and more than three times the uniform-loading value. The low conductivity of the ceramic concentrates the temperature drop in the ceramic-rich upper part, so the metal-rich lower part, which carries most of the membrane stiffness, stays cooler. For $k = 0$ the LHTD and NHTD values coincide, as they must. For $k \geq 5$ the porous plates have a higher ΔT_{cr} than the perfect plate: porosity reduces the plate stiffness and the hygrothermal force in nearly the same proportion, while the foundation contribution is unchanged and therefore weighs more.

Table 8: Critical temperature rise ΔT_{cr} (K) for the three hygrothermal distributions ($a/h = 20$, $\bar{\mu} = 0.02$, $\bar{\ell} = 0.1$, Kerr (100, 10, 100), $\Delta C = 0.2$ wt.%, $T_m = 5$ K).

Porosity	Loading	$k = 0$	$k = 0.5$	$k = 1$	$k = 2$	$k = 5$	$k = 10$
Perfect	UHTR	443.98	261.72	226.06	214.42	234.97	251.07
	LHTD	877.96	533.01	434.75	388.20	415.87	457.97
	NHTD	877.96	939.29	787.54	661.69	595.96	575.48
Even, $e = 0.1$	UHTR	449.15	266.67	231.27	222.05	258.17	294.01
	LHTD	888.30	533.93	431.37	383.36	429.10	504.86
	NHTD	888.30	936.91	775.75	647.22	609.40	630.54
Uneven, $e = 0.1$	UHTR	451.93	268.55	233.85	225.06	255.31	280.76
	LHTD	893.86	544.69	445.34	400.30	440.89	500.40
	NHTD	893.86	953.24	799.37	675.24	626.63	625.77

4.3 Parametric Study

Figures 2–6 use $k = 2$, even porosity $e = 0.1$ and the Kerr foundation (100, 10, 100) unless stated otherwise.

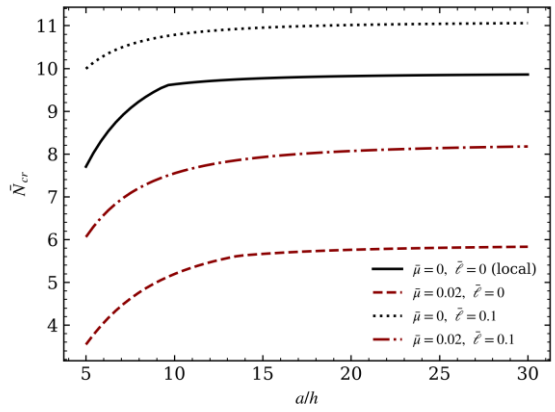


Fig. 2. Effect of the side-to-thickness ratio on $\bar{N}_{cr}$ for four combinations of the nonlocal and strain-gradient parameters (uniaxial load).

The critical load rises with a/h and levels off beyond $a/h \approx 15$, as shear deformation becomes negligible (Fig. 2). The strain-gradient parameter lifts the whole curve and the nonlocal parameter lowers it, with the combined case in between. The kinks near $a/h \approx 10$ and 13 mark a switch of the governing mode from (1, 1) to (2, 1), produced by the foundation, which favours shorter wavelengths.

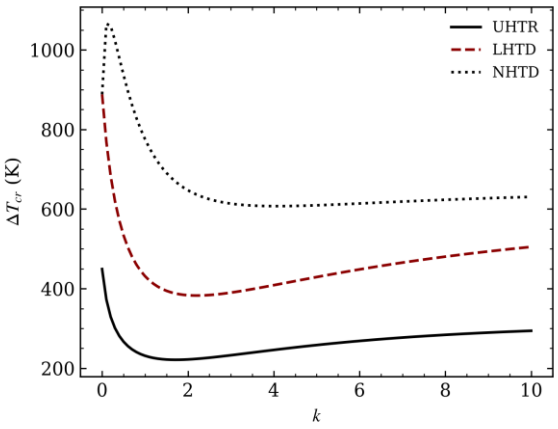


Fig. 3. Critical temperature rise versus the power-law index for the three hygrothermal distributions ($a/h = 20$, $\bar{\mu} = 0.02$, $\bar{\ell} = 0.1$, $\Delta C = 0.2$ wt.%).

Under uniform and linear loading, ΔT_{cr} falls steeply from the ceramic value and reaches a minimum near $k \approx 2$, then rises slowly as the plate becomes metal-rich (Fig. 3). Under nonlinear loading a sharp peak appears at small k ($k \approx 0.2$): the steady conduction profile is then strongly curved, so most of the temperature drop occurs in a thin ceramic-rich layer

and the stiff part of the section stays cool. The choice of thermal profile therefore matters most for plates with a small amount of metal.

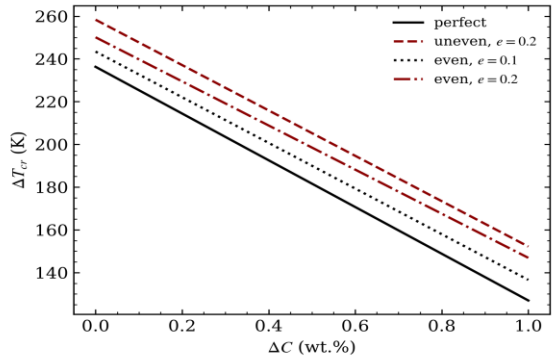


Fig. 4. Critical temperature rise versus moisture concentration for perfect, even-porous and uneven-porous plates (uniform loading, $a/h = 20$, $\bar{\mu} = 0.02$, $\bar{\ell} = 0.1$).

ΔT_{cr} decreases linearly with ΔC, by about 11 K per 0.1 wt.% for the perfect plate (Fig. 4). Moisture and temperature act additively through N^{HT}, so a fixed moisture level shifts the critical temperature by a fixed amount. All curves remain positive up to $\Delta C = 1$ wt.% for this configuration. The porous plates lie slightly above the perfect plate for the reason given under Table 8.

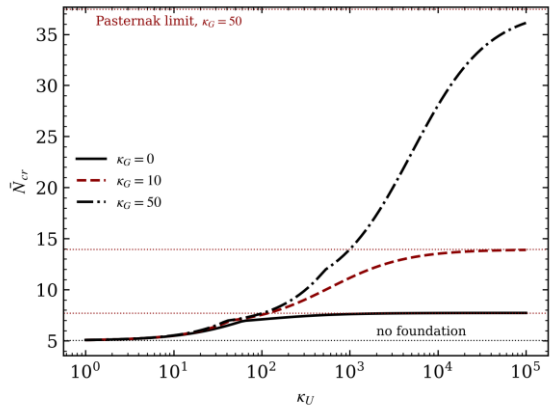


Fig. 5. Critical load versus the upper-spring stiffness of the Kerr foundation for three shear-layer stiffnesses ($\kappa_L = 100$, $a/h = 10$, $\bar{\mu} = 0.02$, $\bar{\ell} = 0.1$). Dotted lines are the no-foundation and Pasternak limits.

The Kerr model spans the full range between no foundation ($\kappa_U \to 0$) and the Pasternak foundation ($\kappa_U \to \infty$), as shown in Fig. 5. The transition occurs between $\kappa_U \approx 10$ and 10^4. A stiffer shear layer needs a stiffer upper layer to develop its full effect: for $\kappa_G = 50$ the Pasternak limit is barely reached at $\kappa_U = 10^5$. Treating a real substrate as Pasternak when its upper layer is compliant can therefore overestimate the critical load several times.

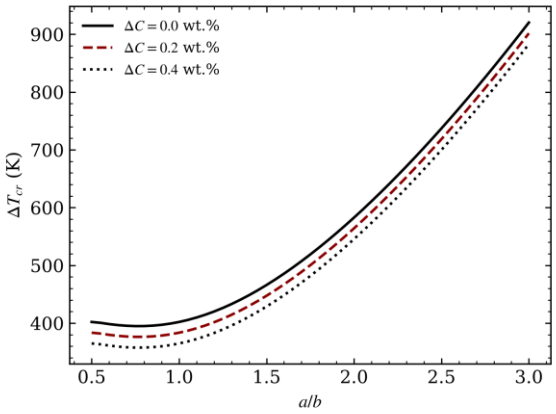


Fig. 6. Critical temperature rise versus aspect ratio a/b for three moisture concentrations (linear loading, $a/h = 20$, $\bar{\mu} = 0.02$, $\bar{\ell} = 0.1$).

With a and h fixed, increasing a/b narrows the plate, and ΔT_{cr} increases steadily beyond a minimum near $a/b \approx 0.8$ (Fig. 6). Moisture shifts the curves down almost uniformly, by about 18 K for each 0.2 wt.%.

5. Conclusions

The hygrothermal and mechanical buckling of porous FG nanoplates on a Kerr foundation was solved in closed form with a one-variable first-order theory written about the physical neutral surface and combined with the nonlocal strain gradient theory. The main conclusions are:

1. Writing the kinematics about the neutral surface removes the stretching–bending coupling and allows the first-order theory of FG and porous FG plates to be reduced exactly to one unknown.
2. The relation between the shear and bending deflections is unchanged by the nonlocal strain gradient operators, so the size-dependent problem is governed by a single equation.
3. The solution reproduces the thermal-buckling results of [6] to all reported digits and agrees closely with the mechanical results of [7] over the whole range of power-law indices, with one unknown instead of three to six.
4. The nonlocal and strain-gradient parameters act as a single multiplier $(1 + \ell^2\alpha^2)/(1 + \mu\alpha^2)$ on the plate stiffness: the plate softens when $\mu > \ell^2$ and hardens otherwise. The foundation term

is not scaled, so foundations matter more for strongly nonlocal plates and can shift the buckling mode.

5. Even porosity reduces the critical load far more than uneven porosity: for $e = 0.2$ the even-porous plate keeps about three-fifths of the perfect-plate load, the uneven-porous plate nearly nine-tenths. Because porosity lowers stiffness and hygrothermal force together, porous plates on a foundation can show a slightly higher critical temperature than perfect ones.
6. The upper spring layer of the Kerr model can reduce the foundation's effect from that of a Pasternak foundation to almost nothing; idealizing a compliant substrate as Pasternak can overestimate the critical load several times.
7. Moisture lowers the critical temperature linearly, by roughly 9–13 K per 0.1 wt.% for the cases studied; the ceramic plate is insensitive to moisture.
8. The conduction-based nonlinear temperature profile gives critical temperatures two to more than three times those of uniform loading and produces a pronounced peak at small power-law indices.

For aerospace design, the closed-form expressions allow rapid screening of graded thermal-protection and sensing nanoplates against combined thermal and moisture loads. Further work can extend the formulation to other boundary conditions with Levy-type or Ritz solutions, include the pre-buckling bending caused by the hygrothermal moment, and use integral (two-phase) nonlocal models.

Data Availability Statement: The Python code used to generate all results and figures, it is available from the author on reasonable request.

Declaration of Generative AI: Generative AI tools (Gemini) were used exclusively for grammatical checking, stylistic refinement, and linguistic phrasing.

Acknowledgments: The author would like to acknowledge the Deanship of Graduate Studies and Scientific Research, Taif University for funding this work.

Conflicts of Interest: "The author declare no conflicts of interest."

References

[1] M. Koizumi, FGM activities in Japan, Composites Part B 28 (1997) 1–4.
[2] J.N. Reddy, Analysis of functionally graded plates, International Journal for Numerical Methods in Engineering 47 (2000) 663–684.
[3] R. Javaheri, M.R. Eslami, Thermal buckling of functionally graded plates, AIAA Journal 40 (2002) 162–169.
[4] W. Lanhe, Thermal buckling of a simply supported moderately thick rectangular FGM plate, Composite Structures 64 (2004) 211–218.
[5] A.M. Zenkour, M. Sobhy, Thermal buckling of various types of FGM sandwich plates, Composite Structures 93 (2010) 93–102.
[6] H. Yaghoobi, M. Torabi, Exact solution for thermal buckling of functionally graded plates resting on elastic foundations with various boundary conditions, Journal of Thermal Stresses 36 (2013) 869–894.
[7] H.T. Thai, S.E. Kim, Closed-form solution for buckling analysis of thick functionally graded plates on elastic foundation, International Journal of Mechanical Sciences 75 (2013) 34–44.
[8] E. Reissner, The effect of transverse shear deformation on the bending of elastic plates, Journal of Applied Mechanics 12 (1945) A69–A77.
[9] R.D. Mindlin, Influence of rotatory inertia and shear on flexural motions of isotropic, elastic plates, Journal of Applied Mechanics 18 (1951) 31–38.
[10] R.P. Shimpi, Refined plate theory and its variants, AIAA Journal 40 (2002) 137–146.
[11] R.P. Shimpi, H.G. Patel, H. Arya, New first-order shear deformation plate theories, Journal of Applied Mechanics 74 (2007) 523–533.
[12] P.L. Pasternak, New calculation method for flexible substructures on a two-parameter elastic foundation, Gos. Izdat. Literatury po Stroitelstvu i Arkhitekture, Moscow (1954) 1–56.
[13] A.D. Kerr, Elastic and viscoelastic foundation models, Journal of Applied Mechanics 31 (1964) 491–498.
[14] H. Akhavan, Sh.H. Hashemi, H.R.D. Taher, A. Alibeigloo, Sh. Vahabi, Exact solutions for rectangular Mindlin plates under in-plane loads resting on Pasternak elastic foundation. Part I: Buckling analysis, Computational Materials Science 44 (2009) 968–978.
[15] A.M. Zenkour, M.N.M. Allam, M.O. Shaker, A.F. Radwan, On the simple and mixed first-order

theories for plates resting on elastic foundations, Acta Mechanica 220 (2011) 33–46.

[16] A.M. Zenkour, A.F. Radwan, On the simple and mixed first-order theories for functionally graded plates resting on elastic foundations, Meccanica 48 (2013) 1501–1516.

[17] K.S. Sai Ram, P.K. Sinha, Hygrothermal effects on the buckling of laminated composite plates, Composite Structures 21 (1992) 233–247.

[18] A.M. Zenkour, M.N.M. Allam, A.F. Radwan, Effects of hygrothermal conditions on cross-ply laminated plates resting on elastic foundations, Archives of Civil and Mechanical Engineering 14 (2014) 144–159.

[19] A.M. Zenkour, M.N.M. Allam, A.F. Radwan, Effects of transverse shear and normal strains on FG plates resting on elastic foundations under hygro-thermo-mechanical loading, International Journal of Applied Mechanics 6 (2014) 1450063.

[20] A.M. Zenkour, A.F. Radwan, Hygrothermo-mechanical buckling of FGMs plates resting on elastic foundations using a quasi-3D model, Int.J.Computational Methods in Engineering science and Mechanics 20.2(2019) 85-98.

[21] D.G. Zhang, Y.H. Zhou, A theoretical analysis of FGM thin plates based on physical neutral surface, Computational Materials Science 44 (2008) 716–720.

[22] M. Aydogdu, Conditions for functionally graded plates to remain flat under in-plane loads by classical plate theory, Composite Structures 82 (2008) 155–157.

[23] N. Wattanasakulpong, V. Ungbhakorn, Linear and nonlinear vibration analysis of elastically restrained ends FGM beams with porosities, Aerospace Science and Technology 32 (2014) 111–120.

[24] D. Chen, J. Yang, S. Kitipornchai, Elastic buckling and static bending of shear deformable functionally graded porous beams, Composite Structures 133 (2015) 54–61.

[25] A.C. Eringen, On differential equations of nonlocal elasticity and solutions of screw dislocation and surface waves, Journal of Applied Physics 54 (1983) 4703–4710.

[26] J.N. Reddy, Nonlocal theories for bending, buckling and vibration of beams, International Journal of Engineering Science 45 (2007) 288–307.

[27] R. Aghababaei, J.N. Reddy, Nonlocal third-order shear deformation plate theory with application to bending and vibration of plates, Journal of Sound and Vibration 326 (2009) 277–289.

[28] A.M. Zenkour, M. Sobhy, Nonlocal elasticity theory for thermal buckling of nanoplates lying on Winkler–Pasternak elastic substrate medium, Physica E 53 (2013) 251–259.

[29] C.W. Lim, G. Zhang, J.N. Reddy, A higher-order nonlocal elasticity and strain gradient theory and its applications in wave propagation, Journal of the Mechanics and Physics of Solids 78 (2015) 298–313.

[30] L. Li, Y. Hu, Buckling analysis of size-dependent nonlinear beams based on a nonlocal strain gradient theory, International Journal of Engineering Science 97 (2015) 84–94.

[31] F. Ebrahimi, M.R. Barati, Hygrothermal effects on vibration characteristics of viscoelastic FG nanobeams based on nonlocal strain gradient theory, Composite Structures 159 (2017) 433–444.

[32] B. Karami, D. Shahsavari, M. Janghorban, L. Li, Free vibration analysis of FG nanoplate with poriferous imperfection in hygrothermal environment, Structural Engineering and Mechanics ,An International journal 73.2(2020)191-207.

[33] D. Shahsavari, B. Karami, H.R. Fahham, L. Li, On the shear buckling of porous nanoplates using a new size-dependent quasi-3D shear deformation theory, Acta Mechanica 229(11) (2018) 4549-4573.

[34] H. Benachi, et al, Instability behavior of FG nanoplates resting on nonlinear Kerr foundations under hygro-thermo-mechanical load using nonlocal elasticity theory, Mechanics of Solids (2025) 7085-7109.

[35] A. Mottaghi, et al, Free vibration analysis of a functionally graded porous nanoplate in a hygrothermal environment resting on an elastic foundation, Forces in Mechanics 17 (2024) 100294.

[36] M. Malikan, V.B. Nguyen,Buckling analysis of piezo-magnetoelectric nanoplates in hygrothermal environment based on a novel one variable plate theory combining with higher-order nonlocal strain gradient theory, Physica E:Low-dimensional systems and Nanostructures 102 (2018) 8-28.